Hydrogen Storage Performance of Preferentially Oriented Mg/rGO Hybrids

Chaochao Dun[1*], Sohee Jeong[1,2*], Deok-Hwang Kwon[3,4], ShinYoung Kang[5], Vitalie Stavila[6], Zhuolei Zhang[1], Joo-Won Lee[2], Tracy M. Mattox[1], Tae Wook Heo[5], Brandon C. Wood[5], and Jeffrey J. Urban[1]

[1] The Molecular Foundry, Lawrence Berkeley National Laboratory Berkeley, Berkeley, CA, 94720, USA

[2] Materials Architecturing Research Center, Korea Institute of Science and Technology, Seoul, 02792, South Korea

[3] Department of Materials Science and Engineering, University of California Berkeley, Berkeley, CA, 94720, USA

[4] Materials Sciences Division, Lawrence Berkeley National Laboratory, Berkeley, CA, 94720, USA

[5] Materials Science Division and Laboratory for Energy Applications of the Future (LEAF), Lawrence Livermore National Laboratory, Livermore, CA, 94550, USA

[6] Energy Nanomaterials Department, Sandia National Laboratories, Livermore, CA, 94550, USA

Corresponding authors: kang10@llnl.gov; jjurban@lbl.gov

Abstract

Chemical interactions on the surface of a functional nanoparticle are closely related to its crystal facets, which can regulate the corresponding energy storage properties like hydrogen absorption. In this study, we reported a one-step growth of magnesium (Mg) particles with both close- and non-close-packed facets, i.e., {0001} and {2$\bar{1}\bar{1}$6} planes, on atomically thin reduced graphene oxide (rGO). The detailed microstructures of Mg/rGO hybrids were revealed by X-ray diffraction, selected-area electron diffraction, high-resolution transmission electron microscopy and fast Fourier transform analysis. Hydrogen storage performance of Mg/rGO hybrids with different orientations varies: Mg with preferential high index {2$\bar{1}\bar{1}$6} crystal surface shows remarkably increased hydrogen absorption up to 6.2 wt% compared with the system exposing no preferentially oriented crystal surfaces showing inferior performance of 5.1 wt% within the first two hours. First-principles calculations revealed improved hydrogen sorption properties on {2$\bar{1}\bar{1}$6} surface with a lower hydrogen dissociation energy barrier and higher stability of hydrogen atoms than those on the {0001} basal plane, supporting the hydrogen uptake experiment. In addition, the hydrogen penetration energy barrier is found to be much lower than that of {0001} due to low surface atom packing density, which might be the most critical process to the

hydrogenation kinetics. The experimental and calculation results present a new handle for regulating hydrogen storage of metal hydrides by controlled Mg facets.

Introduction

Hydrogen is widely considered a promising alternative energy carrier due to the continuous depletion of fossil energy sources and severe environmental destruction[1,2]. Given that the hydrogen economy will necessarily offer a potential solution of a less-polluted environment, technologies related to hydrogen delivery, storage, and production are in high demand. The development of efficient hydrogen storage materials is essential for both mobile and stationary power systems[3,4], which motivates intensive research into solid-state storage technologies. In particular, magnesium (Mg) has been studied as hydrogen storage media due to the advantages of high abundance, non-toxicity, and high gravimetric capacity (7.6 wt%). However, its high thermodynamic stability and high kinetic barriers limit its use as a long-term on-board hydrogen storage material[5,6]. In order to reduce the hydrogenation/dehydrogenation temperature and enhance the kinetics, numerous synthetic approaches have been developed to prepare Mg, including encapsulation[7–9], catalysis[10–13], and nanostructuring[14,15]. For example, we previously reported crystalline Mg/Poly(methyl methacrylate) composites that were relatively air-stable by encapsulating Mg particles in a polymer with selective gas permeability. As a result, rapid uptake of hydrogen was achieved with an enhanced hydrogen capacity (~ 6 wt%) in the absence of a heavy-metal catalyst[7]. Owing to the grain size effect, nanostructured Mg-based materials also exhibit enhanced hydrogenation kinetics.

On the other hand, hydrogen penetration from the outer surface to the internal core crossing the packed planes of metals plays a key role for hydrogen sorption behaviors. As a result, the synthesis of materials with preferential orientation becomes promising. For example, studies of hydrogen ab/desorption on palladium have revealed that the initial desorption rate was nearly ten-fold faster for samples with exclusively {100} facets compared to those with {111} surfaces[16]. Adsorption of hydrogen on nickel single crystal also has various energy barriers depending on its surface orientations[17]. Similarly, hydrogen sorption performance influenced by the surface orientation has been studied by Zhao *et al.* using the first-principles calculations[18].

While the close-packed planes are the most stable surface orientation, such as {0001} plane of hexagonal closest packed (HCP) Mg crystals, these planes consist of a high density of metal atoms, which have negative effects for the penetration of approaching H atoms. Ouyang *et al.* fabricated Mg films with different orientations via magnetron sputtering, and demonstrated that a mix of (0001) and (10$\acute{1}$3) orientations of Mg films can absorb hydrogen at lower temperature than a pure (0001) orientation due to the lower energy barrier for the penetration of hydrogen atoms on (10$\acute{1}$3) plane[19]. Although magnetron sputtering is cost-effective and user-friendly, the as-fabricated Mg films must be deposited onto a specific substrate, which increases the dead mass and hampers its on-board storage application.

Here, we report a feasible approach to grow preferentially orientated Mg nanoparticles on reduced graphene oxide (rGO) by using different reducing agents based on an adapted Rieke method[7]. By controlling the crystallographic features, the associated activation energies reduced, which is the key kinetic-limiting step for traditional metal hydrides; thus, the hydrogen adsorption performance in Mg/rGO hybrids was greatly improved. Experimental results demonstrated a remarkable increase in the hydrogen absorption for Mg/rGO hybrids with preferred orientation of {2$\acute{1}$ $\acute{1}$6} planes using methylnaphthalene as a reducing agent, proved by a dramatically decreased activation energy around 45.99 kJ/mol, compared to the other ones with no preferentially oriented crystal surfaces fabricated using pyrene. First-principle calculations consistently support the improved sorption properties on the {2$\acute{1}$ $\acute{1}$6} surface compared to the corresponding {0001} facet: lower hydrogen dissociation energy barrier, more stable hydrogen absorption thermodynamics, and reduced hydrogen penetration barrier. The combination of experimental and simulation results paves the way for designing preferentially orientated metal hybrids for hydrogen storage.

Results and Discussion

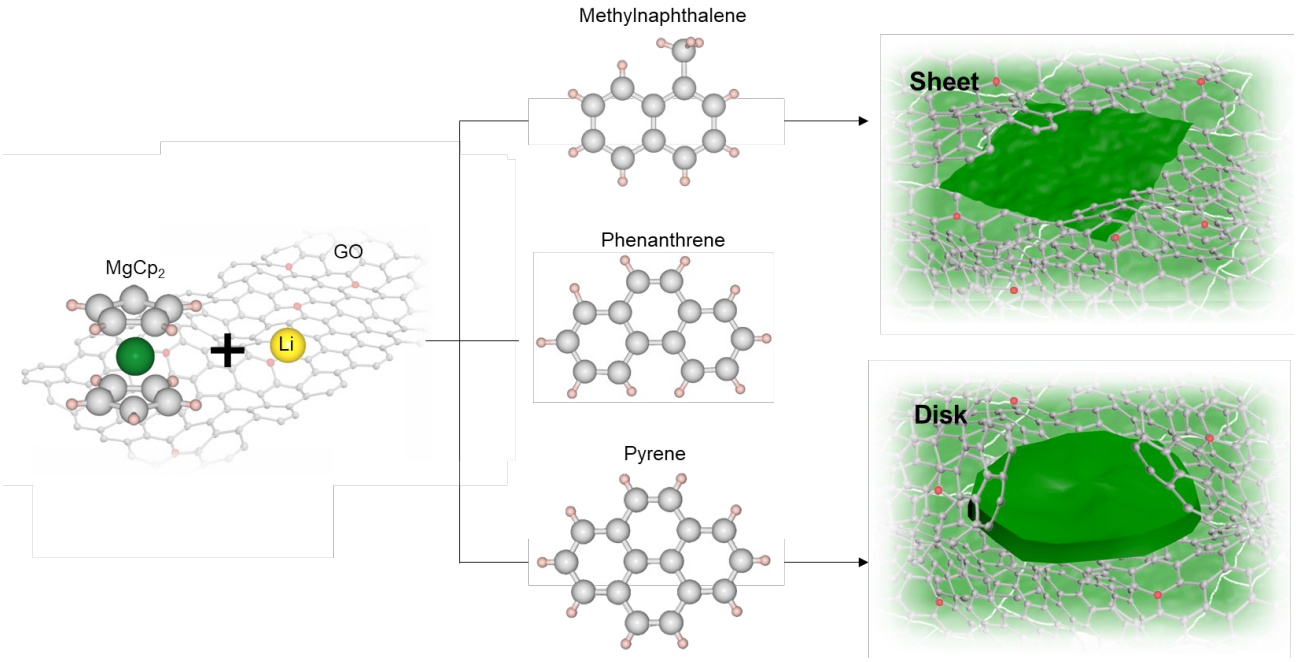

Scheme 1. Synthetic approach to the formation of magnesium particles using different reducing agents.

In order to minimize the inactive mass in the composites, rGO was introduced to confine the particle size of the functional Mg, while maintaining its high phase purity by introducing a protective barrier[9]. Here, three different reducing agents were introduced to control the crystal growth of Mg particles supported by atomically thin rGO under mild conditions: methylnaphthalene, phenanthrene, and pyrene. During the fabrication process, the Mg^{2+} precursor was stabilized by GO, and both were reduced by lithium benzene derivatives to obtain the Mg/rGO composites, as shown in **Scheme 1** (Full details are given in the Experimental Method section). The detailed descriptions on the surface chemistry on single rGO phase with different reducing agents were added in supporting information (**Figure S1**), which confirms that a higher degree of GO reduction was achieved when using methylnaphthalene as a reducing agent compared with the case with pyrene.

The Mg/rGO hybrids obtained using methylnaphthalene, phenanthrene, and pyrene show different shapes and sizes according to transmission electron microscopy (TEM) characterizations (**Figure 1(a)-(c)**). The corresponding hybrids are abbreviated as MMr, PhMr,

and PMr, respectively. The phase purity and structural crystallization of Mg were investigated using powder X-ray diffraction (XRD) in **Figure 1(d)**. The obtained diffraction patterns confirmed that all materials have Mg hexagonal crystal with space group $P6_3/mmc$ without oxidation, supporting successful encapsulation by rGO layers[9]. Interestingly, the (010) Mg peak is relatively strong compared to the (002) peak in MMr. This contrasts with PhMr and PMr where (010) peak is similar to or even slightly weaker than the (002) peak (**Figure 1(d)**). The difference likely arises from the accommodation of preferential orientation of different crystalline planes, which will be shown later.

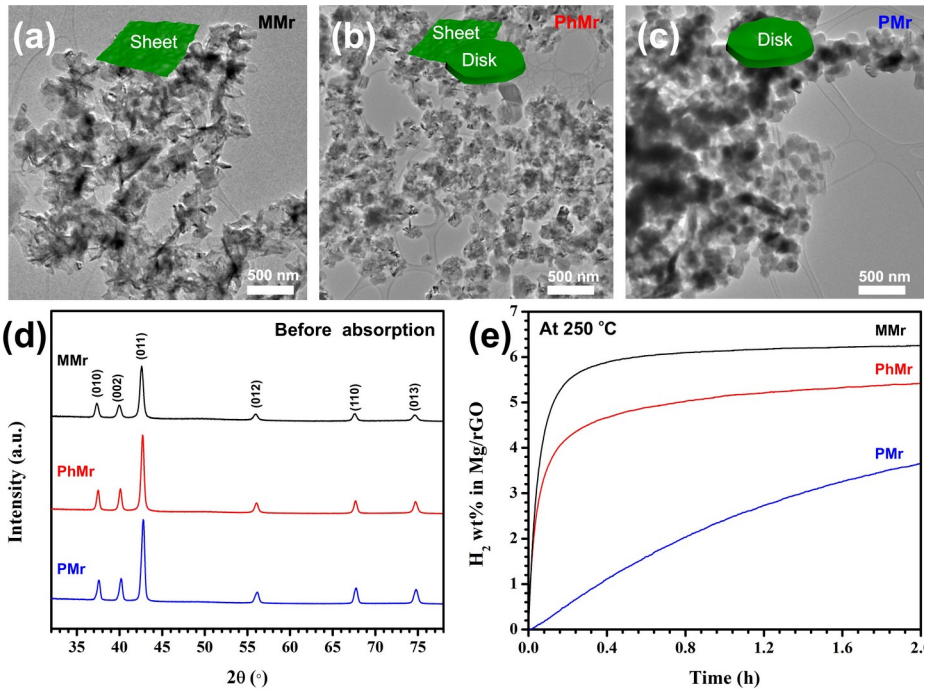

Figure 1. (a-c) Low-magnification TEM images, (d) XRD patterns before hydrogen absorption, and (e) absorption profile at 250 °C, 15 bar of H_2 for Mg/rGO hybrids based on different reducing agents, including methylnaphthalene (black line), phenanthrene (red line), and pyrene (blue line), represented as MMr, PhMr and PMr, respectively.

Hydrogen absorption properties of MMr, PhMr, and PMr composites were examined using a Sieverts PCT-Pro instrument at 250 °C under 15 bar of H_2 (**Figure 1(e)**). The hydrogen absorption data is for the as-prepared samples without activation in order to explore the effect of the preferential orientation of Mg. The hydrogen absorption capacity of the composite is 3.5, 5.1, and 6.2 wt% (calculated on a full composite mass basis) for PMr, PhMr, and MMr, respectively. Among them, MMr displays the best absorption rates compared to PhMr and PMr, in which

hydrogen uptake was immediate. Given the atomically thin and light nature of the encapsulation, the Mg/rGO composites obtained based on methylnaphthalene achieved denser packing of metal nanocrystals and optimized H_2 storage density. In samples containing MMr and PhMr, the nanocomposites readily absorbed hydrogen under mild conditions, unlike bulk Mg or PMr, which require higher temperatures and/or catalysts to achieve hydrogenation. Our previous study showed that rGO layers can prevent O_2 and H_2O penetration while allowing the diffusion of H_2, and rGO in the composite does not provide additional contribution to the hydrogen absorption[9]. XRD results comfirm the formation of magnesium hydride (MgH_2) for all three Mg/rGO samples after hydrogenation (**Figure S2**). It was clearly seen that the diffraction peaks of Mg disappeared whereas diffraction intensity of the MgH_2 peaks became stronger for the MMr sample. In contrast, Mg crystallites were still observed in the PhMr and PMr samples after hydrogenation, suggesting that the hydrogen penetration and bond formation with the internal Mg atoms is more sluggish in these two systems.

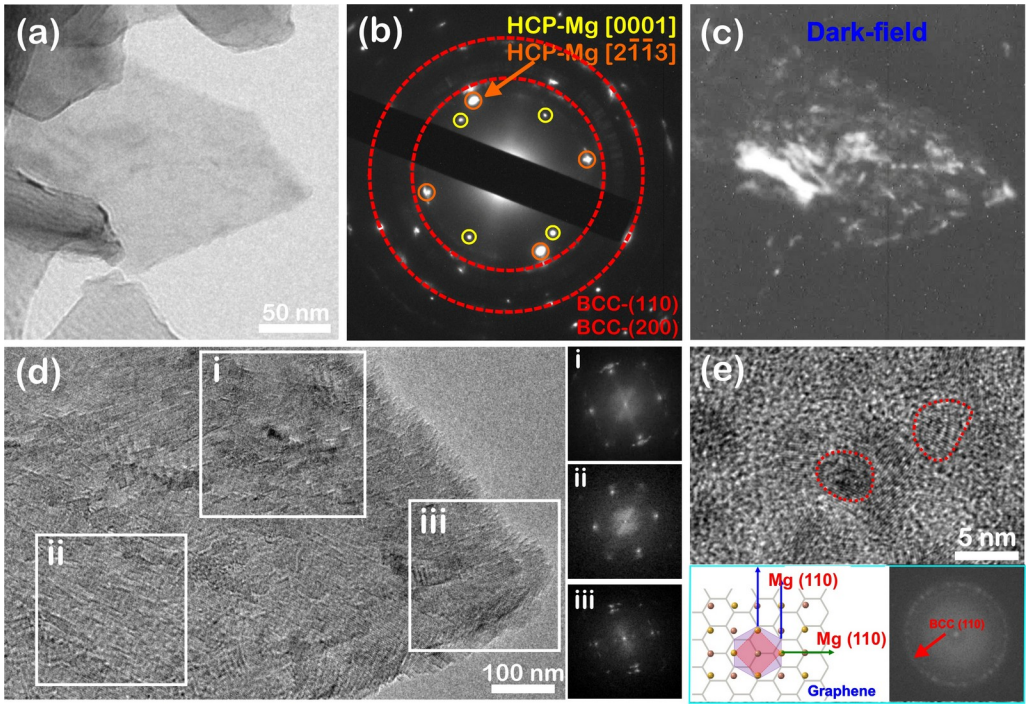

Figure 2. TEM analysis of Mg/rGO synthesized by methylnaphthalene (MMr). (a) Low-magnification TEM image of Mg/rGO sheets, (b) selected-area diffraction pattern taken from the sheet, (c) dark-field image obtained from the diffraction spot pointed by an orange arrow in (b), (d) magnified TEM image of

MMr sheet with the corresponding fast Fourier transformed patterns given in (i-iii), and (e) high-resolution TEM image showing the detailed body-centered cubic Mg particles observed on top of rGO.

To understand the origin of distinct hydrogen uptake behaviors depending on the reducing agents, further structure characterizations were performed on the MMr and PMr composites. Mg sheets were characterized using a selected-area electron diffraction (SAED) pattern, dark-field imaging, high-resolution transmission electron microscopy (HRTEM), and fast Fourier transformed (FFT) analysis. Interestingly, we found that Mg sheets in MMr consist of a large single grain with preferential orientation (i.e., zone axis) with a few small crystallines. **Figure 2(a)** is a low-magnification TEM image showing sheet-like morphology of MMr. The SAED pattern was taken from an area of a few hundred nanometers, from which two large Mg grains were identified. One is marked by yellow, and the other one is marked by orange circles in **Figure 2(b)**. Each orange and yellow circle in **Figure 2(b)** corresponds to the zone-axis of [2$\bar{1}\bar{1}$3]=[101] and [0001]=[001] HCP-Mg, respectively. Note that the non-close-packed [2$\bar{1}\bar{1}$3]=[101] oriented Mg sheets are observed. **Figure 2(c)** is dark-field image of the grains from the electron diffraction peak marked by an orange arrow in **Figure 2(b)** (*i.e.*, an electron diffraction peak from [2$\bar{1}\bar{1}$3]=[101] HCP-Mg grain), demonstrating that the [2$\bar{1}\bar{1}$3] oriented crystalline grains cover the whole area of the Mg flake. Exemplified FFTs in **Figure 2(d)**, taken from three different locations on the Mg sheet, also verifies that [2$\bar{1}\bar{1}$3] oriented HCP-Mg are maintained across the whole part of the sheet. Applying a metric tensor to the Mg-flake orientation of [2$\bar{1}\bar{1}$3], we confirmed that the normal 'plane' of the flake is (2$\bar{1}\bar{1}$6), which is the major facet of the flake exposed to hydrogen. Note that since HCP-Mg is a non-cubic system, the index number of 'plane' is non-proportional to 'direction'. Compared with energetically favorable (0001) planes, the high-index Mg (2$\bar{1}\bar{1}$6) plane is non-close-packed and likely the high energy surface exhibiting more dangling bonds with high reactivity towards hydrogen atoms.

Besides, we observed small crystallites around a few nanometers within the HCP-Mg flake of MMr, which can be identified in the FFT pattern (**Figure 2(d)i-iii)**, electron diffractions other than peaks corresponding to [2$\bar{1}\bar{1}$3] HCP-Mg. The HRTEM image taken from the other flake at the off-axis better demonstrates the existence of these small crystallines, marked by red circles (**Figure 2(e)**). We assign the small crystallines as body-centered cubic (BCC)-Mg rather

than graphene or carbon, since they appear with clear diffraction fringes, unlike the amorphous type of graphene or carbon. It is noteworthy that BCC-Mg is unstable[20], and unlikely to form thermodynamically. Hence, it is considered that BCC-Mg is formed on top of rGO during the early stages of the reaction. Since Mg precursors adsorbed on rGO in the limited time due to rapid reaction of GO reduction, strain energy from the lattice match between BCC-Mg and rGO can dominate rather than the thermodynamic energy of HCP-Mg. Once BCC-Mg crystallites become large enough, they transform into the growth mode to make the thermodynamically stable HCP-Mg and a large size grain sheet develops, as seen in **Figure 2(d)**. Additional HRTEM images of MMr samples may be found in the Supporting Information (**Figure S3**), further supporting the observation of preferentially oriented HCP-Mg sheet as well as the details of the crystallographic feature of the MMr samples.

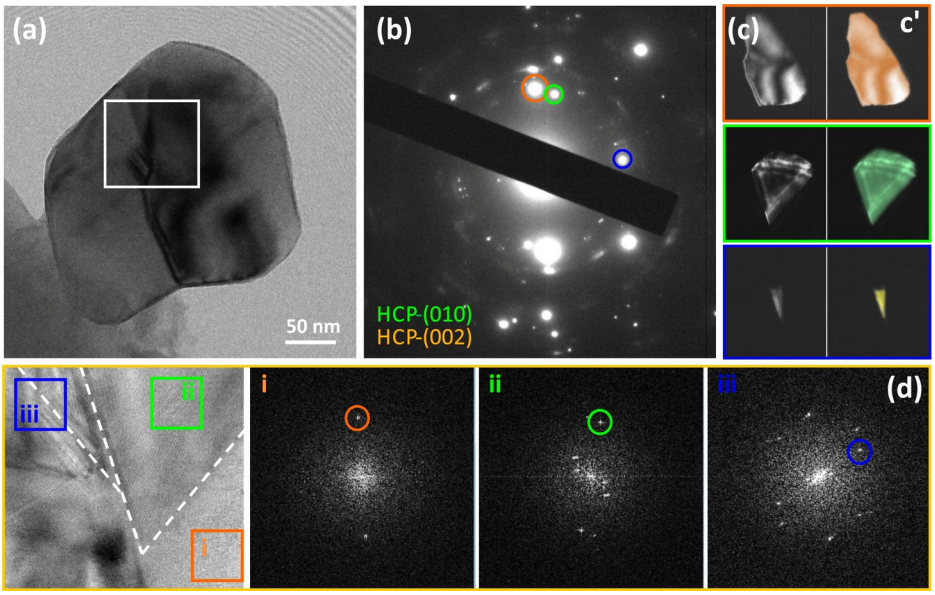

Figure 3. TEM analysis of Mg/rGO synthesized by pyrene (PMr). (a) Low-magnification TEM image of Mg/rGO disc-like particles, (b) selected-area diffraction pattern taken from the disk-like particle, (c) dark-field image obtained from the diffraction spot marked by an orange, green, and yellow circles in the diffraction pattern in (b). The false-colored TEM images as orange, green, and yellow for clear visibility were also given. (d) High-resolution TEM image of Mg/rGO particles, with the fast Fourier transformed patterns (i-iii) corresponding to the orange, green, and yellow solid frames.

On the other hand, Mg particles synthesized by pyrene (PMr) were also characterized by TEM in the same manner applied to the MMr sample. In contrast to MMr, PMr samples contain disk-like particles consisting of multiple grains, as seen in TEM image given in **Figure 3(a)**. On the other hand, note that the morphology of PhMr sample particles is the combination of MMr and PMr samples, showing a mixture of sheet-like and disc shapes. SAED pattern in **Figure 3(b)** shows that electron diffraction pattern consists of several polycrystalline grains with different orientations. This is dramatically different from those observations on the MMr sample, in which a large single grain dominates in Mg flake with preferred orientation. Some diffraction peaks, marked by orange, green, and blue circles, are selected to visualize corresponding grains in dark-field imaging (**Figure 3(c)**). **Figure 3(d)** shows HRTEM image where we could find three different grains, showing different FFTs for each grain different (Figure 3d (i), (ii), and (iii)). These results indicate that Mg particles in PMr consist of multiple grains without preferred orientation. It is also noteworthy that darker contrast of Mg particles in low-magnification image (**Figure 3(a)**) suggests a larger particle thickness[21] in the PMr sample compared to the MMr sample (**Figure 2(a)**), which can be also related to the less competitive H_2 absorption of the PMr sample due to the smaller surface area in a given mass.

Orientation and morphology variations of the present systems suggest the distinguishing Mg formation behavior by using different reducing agents, in which the interaction between radical anions and Mg precursor plays an important role. Here, we hypothesized that that the dramatic different crystal growth phenomenon is related to the synergetic effect of different reducing agents and the combination of reduction rates of Mg ions and graphene oxide (**Figure S1**). To verify the hypothesis, we calculated the relative reduction potentials of methylnaphthalene and phenanthrene radical anions with respect to that of pyrene radical anion ($\square_{pyrene}$), which are $\square_{pyrene}$ + 0.640 V and $\square_{pyrene}$ + 0.464 V, respectively. The calculation details are given in the Calculational Method section. Here, the higher potential of methylnaphthalene suggests that it is more stable as a neutral molecule than as a radical anion. Therefore, methylnaphthalene is prone to donate electrons, facilitating the growth of Mg particles than the other two, forming a non-equilibrium shape of Mg particles populated with the high-energy {2Í Í 6} facets. On the contrary, low redox potential of pyrene may contribute to the formation of Mg

particles, leading to (pseudo-)equilibrium shape with various low-energy surfaces, such as {1̄2 1̄ 0} and {0002} as in **Figure 3(b).** Indeed, we found out that the preferentially orientated Mg/rGO hybrids using methylnaphthalene as reducing agent can be achieved within 5 minutes, which is in agreement with its higher redox potential. The related XRD measurements for MMr with different reaction times were given in **Figure S4**. The correlation between the crystal growth rate and appearing facets was also previously reported: By using voltage as driving force for crystal growth of cobalt, R. Seaki and T. Ohgai found that the high-energy (100) planes or other facets were more dominant than the low-energy (001) orientation at higher overpotential due to the accelerated growth rate of electrodeposited cobalt[22]. In addition, S. Ghosh *et al*. reported the effect of temperature to the growth rate of copper[23], where they observed a higher fractal dimension that is a mixture of high-energy surfaces at higher temperatures. Thermal energy accelerated growth rate of electrodeposited copper by aiding high diffusivity of atoms, leading to a crystal morphology with high-energy surfaces.

In order to investigate the kinetic properties of preferentially orientated Mg/rGO hybrids, hydrogen absorption tests were performed as a function of temperature for MMr (**Figure S5**). A clear absorption trend was observed, in which the wt% hydrogen absorbed by Mg increases with elevated temperature. The activation energy (E_a) for hydrogen absorption was found to be about 45.99 kJ/mol by fitting the result with the Johnson–Mehl–Avrami (JMA) model[24,25]. Remarkably, this value surpasses the best environmentally robust samples made to date, and is much lower than E_a value of Mg particles obtained with naphthalenide (~60.8 kJ/mol)[9], which is a powerful reducing agent as the alkali metals[21]. This result is even comparable to transition metal-catalyzed bulk metal-hydride system[27]. This large performance enhancement can be attributed to the orientation-dependent hydrogen absorption behavior as confirmed by the *ab initio* calculations below.

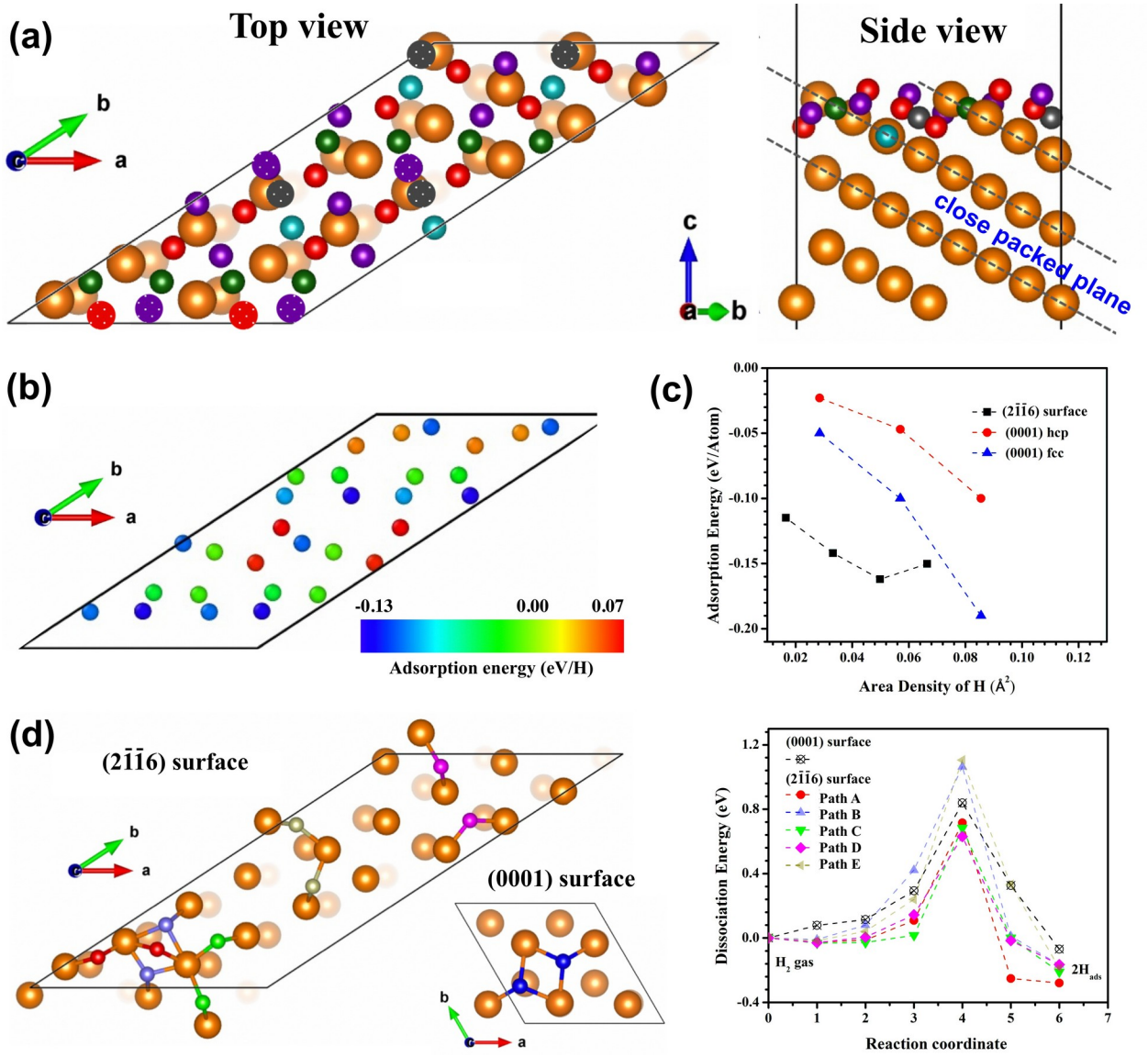

Figure 4. (a) Configuration of Mg (2$\bar{1}\bar{1}$6) slab with possible H adsorption sites. Mg atoms are large orange spheres and H adsorption sites are color-coded by their site properties (see text). (b) Calculated adsorption energy, E_{ads}, of single H adatom on the (2$\bar{1}\bar{1}$6) surface referencing to H_2 gas. (c) The relationship of E_{ads} with different area densities of H atoms, with comparisofrom previous reference for the (0001) plane (Permission to reuse from APS physics)[28]. (d) Nudged elastic band (NEB) energy profiles for the H_2 dissociation reactions on Mg (0001) and (2$\bar{1}\bar{1}$6) surfaces along with their final two adsorbed atoms ($2H_{ads}$) configurations. Dissociated, adsorbed H atoms are depicted by blue spheres for the (0001) surface, while the $2H_{ads}$ pairs on the (2$\bar{1}\bar{1}$6) surface follows the colors of their energy profiles.

Finally, first-principles calculations were conducted to clarify the role of high-index (2$\bar{1}\bar{1}$6) surface to the improved hydrogen storage performance in the MMr system. Energies of hydrogen dissociation, surface adsorption and diffusion, and penetration processes were calculated on the Mg (2$\bar{1}\bar{1}$6) surface compared with the (0001) surface. **Figure 4(a)** shows the (2$\bar{1}\bar{1}$6) surface expanded twice in the *a*-direction along with the possible adsorption sites for hydrogen: Octahedral interstitial sites are in red, tetrahedral interstitial sites are in purple, bridge sites between two surface Mg atoms are in green, sites on top of surface Mg atoms are in gray, and hollow sites where hydrogen is at C sites from ABAB-stacked hcp lattice are in cyan. The calculated adsorption energies E_{ads} are displayed in **Figure 4(b)**. A few potential adsorption sites considered in this study were relaxed to adjacent low-energy sites, for example, all *top* sites. These sites are depicted by patterned spheres in **Figure 4(a)** and excluded from **Figure 4(b)**. On the (2$\bar{1}\bar{1}$6) surface, the adsorption energy of a single H adatom is as low as -0.12 eV, indicating much higher stability compared to the (0001) surface with -0.05 eV[29]. Such hydrogen stability is further extended to higher H coverage: As in **Figure 4(c)**, up to ~0.07 $Å^{-2}$ area density of hydrogen, the (2$\bar{1}\bar{1}$6) surface has lower adsorption energy than the (0001) surface. Note that 0.07 $Å^{-2}$ area density corresponds to ~ 1 ML for the (2$\bar{1}\bar{1}$6) surface, while only 0.5 ML for the (0001) surface.

Table 1. Summary of calculated energy barriers in eV for H_2 gas to $2H_{ads}$ dissociative adsorption (E_b), surface diffusion (E_d) and penetration (E_p) on the Mg (2$\bar{1}\bar{1}$6) and (0001) surfaces.

In eV	Dissociation E_b	Surface Diffusion E_d	Penetration E_p
(2$\bar{1}\bar{1}$6)	0.63-1.11	0.03-0.46	0.23-0.43
(0001)	0.84, 0.75±0.15[30], 1.10[31], 0.87[29], 1.15[32]	~0.18[29]	0.46-0.78[19]

Kinetics of hydrogen-Mg (2$\bar{1}\bar{1}$6) surface interaction was further assessed by calculating the energy barriers for H_2 dissociation, surface diffusion, and penetration to subsurface. **Figure 4(d)** shows the nudged elastic band (NEB) energy profiles for the H_2 dissociation reactions on Mg (0001) and (2$\bar{1}\bar{1}$6) surfaces, demonstrating that there are multiple pathways on the (2$\bar{1}\bar{1}$6)

surface with lower energy barriers than the (0001) surface as well as $(10\bar{1}3)$ surface[19]. More detials were given in **Figure S6**. Note that the $(2\bar{1}\bar{1}6)$ surface is non-close-packed plane with high surface energy (0.75 J/m^2), while the (0001) surface is close-packed, most stable surface (0.60 J/m^2). To accommodate more hydrogen and vacate reactive surface sites, dissociative adsorption should be followed by surface diffusion. A few pathways of hydrogen diffusion on the $(2\bar{1}\bar{1}6)$ surface were sampled by connecting two low-E_{ads} sites, or one low-E_{ads} and one mid-E_{ads} site from **Figure 1(b)**. The sampled pathways are displayed in **Figure S6**. The diffusion energy barrier between two low-energy sites were relatively high of 0.42-0.46 eV, compared to the hydrogen diffusion energy barrier of 0.18 eV on the (0001) surface [29]. However, diffusion pathways with much smaller barrier energy of 0.03-0.28 eV are also accesisble between the low-E_{ads} site and mid-E_{ads} site (T-O and T-T paths in **Figure S6**), suggesting that the non-close-packed $(2\bar{1}\bar{1}6)$ surface offers uneven energy landscape with a few facile diffusion pathways for hydrogen.

Similarly, hydrogen penetration energy barriers from surface to subsurface were computed for selected surface-subsurface site pairs. **Figure S7** shows the diffusion pathways considered in this study along with the energy of hydrogen on surface and subsurface sites. In general, hydrogen is more stable on the surface than the subsurface, providing lower penetration energy barriers for hydrogen than its outward diffusion from subsurface to surface. We found the hydrogen penetration energy barriers are 0.23-0.43 eV on the $(2\bar{1}\bar{1}6)$ surface, which is substantial lower than the penetration energy barrier on the (0001) surface, 0.46-0.78 eV[19]. Considering the activation energy obtained using the uptake isotherms and JMA model in **Figure S5** has more weights from the later stage of absorption, the penetration energy barrier lowered from 0.46-0.78 eV on the (0001) surface to 0.23-0.43 eV on the $(2\bar{1}\bar{1}6)$ surface is in good match with the reduction of activation energy from > 60 kJ/mol to 45.99 kJ/mol.

The calculated energy barriers for H_2 dissociative adsorption, surface diffusion and penetration on the Mg $(2\bar{1}\bar{1}6)$ surface along with the reference (0001) surface are summarized in **Table 1**. Collectively, our DFT computation revealed that the $(2\bar{1}\bar{1}6)$ surface offers low-energy barrier pathways for hydrogen dissociative adsorption, surface diffusion, and penetration besides

higher thermodynamic stability of adsorption. Ouyang *et al.* attributed the lower kinetic energy barriers and high adsorbed hydrogen stability on a non-close-packed surface to the lower bonding energies between surface Mg atoms and high surface energies[19]. We further confirmed that the low area density of surface Mg atoms induces uneven energy landscape, which diversify diffusion energy barriers including the ones accessible with < 0.2-0.3 eV for both surface diffusion and penetration. Easier and deeper penetration of hydrogen to the interior region and none-close-packed orientation of particles may facilitate the phase transformation to MgH_2 supporting the faster hydrogenation of the Mg-rGO hybrids synthesized with methylnaphthalene (MMr) as observed in **Figure 1(e).**

Conclusions

A single crystalline Mg sheet with a preferred orientation of $\{2\bar{1}\bar{1}6\}$ was fabricated on rGO based on a facile wet-chemical method using methylnaphthalene as a reducing agent. The orientation and morphology variations of the present system are closely related to the reducing strength of the reducing agents. We found out that methylnaphthalene has the highest relative redox potential, which tends to donate electron and results in the fastest growth rate for Mg particles. The Mg/rGO hybrids with a non-close-packed $\{2\bar{1}\bar{1}6\}$ orientation shows much improved hydrogen absorption, which is the key limiting step for traditional metal hydrides, with the activation energy (E_a) of ~45.99 kJ/mol. First-principles calculations attributed this to the fact that the non-close-packed plane of Mg $(2\bar{1}\bar{1}6)$ generates uneven energy landscape, and offers facile kinetic pathways for hydrogen dissociation, diffusion, and penetration. In addition, the high surface energy of Mg $(2\bar{1}\bar{1}6)$ stabilizes hydrogen absorption thermodynamics, indicating improved thermodynamics and kinetics of hydrogen absorption on the $(2\bar{1}\bar{1}6)$ surface compared to the (0001) surface. By combining the experiment and simulation, our work provides fundamental insights to design novel metal hydrides with better hydrogen storage performance.

Experimental Method

Bis(cyclopentadienyl)magnesium (> 99.99%) and tetrahydrofuran (THF) were purchased from Sigma-Aldrich. Single layer graphene oxide was purchased from ACS Material. Lithium foil (99%) was purchased from Alfa Aesar. Methylnaphthalene, phenanthrene and pyrene were purchased from Sigma-Aldrich. Lithium methylnaphthalene (phenanthrene or pyrene) solutions were prepared by dissolving 18.5 mmol methylnaphthalene in THF (120 mL), followed by the addition of Li metal (27.2 mmol, 0.189 g). GO (6.56 mg) was dispersed in THF (13.1 mL), sealed in a glove box and sonicated for 1.5 h. Bis(cyclopentadienyl)magnesium (15 mmol, 2.31 g) were dissolved in THF (22.5 mL) and the solution was added into the GO solution and then stirred for 30 min. The combined solution was mixed with the lithium methylnaphthalene solution, then stirred for another 2 h. The resultant suspension was centrifuged for 20 min at 10000 rpm and washed with THF twice (10000 rpm, 20 min) to remove the residual reagents. The as-prepared nanoparticles were completely dried under vacuum overnight before testing.

X-ray photoelectron spectroscopy (XPS, Thermo Fisher, USA) measurements were conducted to analyze the chemical states of the rGO during the reducing process. The photoelectron spectrometer system was configured with an Al K_α excitation source with spot size of 400 μm. Before collecting XPS spectrum, ion flood source was adopted for charge neutralization. High-resolution TEM images were obtained with JEOL 2100-F Field-Emission Analytical Transmission Electron operated at 200 kV and with Philips CM300FEG/UT at 300 kV. XRD patterns were obtained with a Bruker AXS D8 Discover GADDS X-Ray Diffractometer, using Co Kα radiation (λ = 0.179 nm). Hydrogen absorption kinetic measurements were conducted using a Sieverts PCT Pro-2000 at 15 bar/0 bar of hydrogen at different temperatures. The Pressure-Composition-Temperature (PCT, Setaram PCTPro instrument) measurement was performed to check the hydrogen storage of Mg/rGO hybrids. For each testing, 120 mg of Mg-rGO sample was used. The hydrogen absorption data is for the as-prepared samples without activation in order to explore the effect of the preferential orientation of Mg, while the activation energy is calculated based on the activated samples as the activation process is important before hydrogen storage kinetics tests, especially for the solvent-based systems.

Calculational Method

The calculation of relative redox potential for different reducing agents was performed using NWChem software [33] with basis set (6-31+G*) in B3LYP theory.[34] The electron affinity (EA was determined based on the difference between energy of neutral molecule (E(X)) and energy of radical anion (E($X^{\bullet-}$)): EA=E(X)- E($X^{\bullet-}$). Based on which, the redox potential is calculated,

$$\text{Redox Potential}=-\text{EA}/F= -(E(\text{X})- E(\text{X}^{\bullet-}))/F$$

where F is Faradays' constant. Given that the redox potential is calculated based on the gas phase neutral molecule and radical anion, direct comparison with the standard hydrogen electrode (SHE) values where the solvated ions involve is not applicable. Therefore, we utilized the calculated redox potential to provide the relative reducing power of methylnaphthalene and phenanthrene with respect to that of pyrene.

Density Functional Theory (DFT) calculations were performed using the Vienna *ab initio* Simulation Package (VASP)[35]. Generalized gradient approximation (GGA) parametrized by Perdew-Burke-Ernzerhof (PBE)[36] were used for the exchange-correlation functional, and eight valence electrons for Mg were accounted in the projector-augmented wave (PAW) potentials[37] The plane-wave energy cutoff was set to 520 eV. The (2$\bar{1}$1$\bar{6}$) surface slab was constructed using the Atomic Simulation Environment (ASE) code package [38], which has the simulation box dimension of a=5.524 Å, b=19.827 Å, and γ=33.30°. Slab thickness was ~15 Å with the comparable vacuum thickness. The simulation cell was fixed while the atomic positions were relaxed until the energy and force converges less than 10^{-7} eV and 0.005 eV/Å, respectively. A gamma-centered 4×1×1 grid was used for the k-point sampling. Hydrogen absorption energy was calculated with respect to the total energy of bulk HCP Mg and H_2 gas:

$$E_{ads} = E_{total}(\text{nMg-H}_{ads}) - n\, E_{total}\,(\text{bulk hcp Mg}) - \tfrac{1}{2}\, E_{total}\,(H_2\ \text{gas})$$

where E_{total}(A) is the total energy of system A, n is the number of Mg atoms in the H adsorbed system. For the climbing image nudged elastic band (NEB) calculations[39], the (2$\bar{1}$1$\bar{6}$) surface unit cell was expanded twice in the a-direction. Five images for H_2 dissociative adsorption and three images for surface diffusion and penetration were used between the initial and final configurations with a force tolerance of 0.05 eV/Å.

Acknowledgements

Dr. Chaochao Dun and Dr. Sohee Jeong contributed equally to this work. The authors appreciate the support from the Molecular Foundry, Lawrence Berkeley National Laboratory. This work was performed under the support from the Hydrogen Materials Advanced Research Consortium (HyMARC), established as part of the Energy Materials Network by the U.S. Department of Energy (DOE), Office of Energy Efficiency and Renewable Energy, Office of Science, Office of Basic Energy Sciences, Fuel Cell Technologies Office, under Contract No. DE-AC02-05CH11231. This work was also performed under the auspices of the DOE by Lawrence Livermore National Laboratory (LLNL) under contract DE-AC52-07NA27344, and by the Materials Innovation Project (NRF-2020M3H4A3081791) funded by National Research Foundation of Korea and the Future Key Technology Program (Project No. 2E31181) funded by the Korea Institute of Science and Technology. This work was supported by the Laboratory Directed Research and Development (LDRD) program at Sandia National Laboratories. Sandia National Laboratories is a multimission laboratory managed and operated by National Technology and Engineering Solutions of Sandia, LLC., a wholly owned subsidiary of Honeywell International, Inc., for the U.S. Department of Energy's National Nuclear Security Administration under contract DE-NA-0003525.

References

(1) Preuster, P.; Alekseev, A.; Wasserscheid, P. Hydrogen Storage Technologies for Future Energy Systems. *Annu. Rev. Chem. Biomol. Eng.* **2017**, *8*, 445–471.

(2) Midilli, A.; Ay, M.; Dincer, I.; Rosen, M. A. On Hydrogen and Hydrogen Energy Strategies: I: Current Status and Needs. *Renew. Sustain. Energy Rev.* **2005**, *9* (3), 255–271.

(3) Schlapbach, L.; Züttel, A. Hydrogen-Storage Materials for Mobile Applications. *Nature* **2001**, *414*, 353–358.

(4) Schneemann, A.; White, J. L.; Kang, S.; Jeong, S.; Wan, L. F.; Cho, E. S.; Heo, T. W.; Prendergast, D.; Urban, J. J.; Wood, B. C.; Allendorf, M. D.; Stavila, V. Nanostructured Metal Hydrides for Hydrogen Storage. *Chem. Rev.* **2018**, *118* (22), 10775–10839.

(5) Yartys, V. A.; Lototskyy, M. V.; Akiba, E.; Albert, R.; Antonov, V. E.; Ares, J. R.; Baricco, M.; Bourgeois, N.; Buckley, C. E.; Bellosta von Colbe, J. M.; Crivello, J. C.; Cuevas, F.; Denys, R. V.; Dornheim, M.; Felderhoff, M.; Grant, D. M.; Hauback, B. C.; Humphries, T. D.; Jacob, I.; Jensen, T. R.; de Jongh, P. E.; Joubert, J. M.; Kuzovnikov, M. A.; Latroche, M.; Paskevicius, M.; Pasquini, L.; Popilevsky, L.; Skripnyuk, V. M.; Rabkin, E.; Sofianos, M. V.; Stuart, A.; Walker, G.; Wang, H.; Webb, C. J.; Zhu, M. Magnesium Based Materials for Hydrogen Based Energy Storage: Past, Present and Future. *Int. J. Hydrogen Energy* **2019**, *44* (15), 7809–7859.

(6) Andersson, J.; Grönkvist, S. Large-Scale Storage of Hydrogen. *Int. J. Hydrogen Energy* **2019**, *44*, 11901–11919.

(7) Jeon, K. J.; Moon, H. R.; Ruminski, A. M.; Jiang, B.; Kisielowski, C.; Bardhan, R.; Urban, J. J. Air-Stable Magnesium Nanocomposites Provide Rapid and High-Capacity Hydrogen Storage without Using Heavy-Metal Catalysts. *Nat. Mater.* **2011**, *10* (4), 286–290.

(8) Ruminski, A. M.; Bardhan, R.; Brand, A.; Aloni, S.; Urban, J. J. Synergistic Enhancement of Hydrogen Storage and Air Stability via Mg Nanocrystal-Polymer Interfacial Interactions. *Energy Environ. Sci.* **2013**, *6*, 3267–3271.

(9) Cho, E. S.; Ruminski, A. M.; Aloni, S.; Liu, Y. S.; Guo, J.; Urban, J. J. Graphene Oxide/Metal Nanocrystal Multilaminates as the Atomic Limit for Safe and Selective Hydrogen Storage. *Nat. Commun.* **2016**, *7*, 10804.

(10) House, S. D.; Vajo, J. J.; Ren, C.; Rockett, A. A.; Robertson, I. M. Effect of Ball-Milling Duration and Dehydrogenation on the Morphology, Microstructure and Catalyst Dispersion in Ni-Catalyzed MgH_2 Hydrogen Storage Materials. *Acta Mater.* **2015**, *86*, 55–68.

(11) Jia, Y.; Sun, C.; Peng, Y.; Fang, W.; Yan, X.; Yang, D.; Zou, J.; Mao, S. S.; Yao, X. Metallic Ni Nanocatalyst in Situ Formed from a Metal-Organic-Framework by Mechanochemical Reaction for Hydrogen Storage in Magnesium. *J. Mater. Chem. A* **2015**, *3* (16), 8294–8299.

(12) Xie, L.; Liu, Y.; Zhang, X.; Qu, J.; Wang, Y.; Li, X. Catalytic Effect of Ni Nanoparticles on the Desorption

Kinetics of MgH2 Nanoparticles. *J. Alloys Compd.* **2009**, *482*, 388–392.

(13) Hanada, N.; Ichikawa, T.; Fujii, H. Catalytic Effect of Nanoparticle 3d-Transition Metals on Hydrogen Storage Properties in Magnesium Hydride MgH2 Prepared by Mechanical Milling. *J. Phys. Chem. B* **2005**, *109* (15), 7188–7194.

(14) Li, W.; Li, C.; Ma, H.; Chen, J. Magnesium Nanowires: Enhanced Kinetics for Hydrogen Absorption and Desorption. *J. Am. Chem. Soc.* **2007**, *129* (21), 6710–6711.

(15) Norberg, N. S.; Arthur, T. S.; Fredrick, S. J.; Prieto, A. L. Size-Dependent Hydrogen Storage Properties of Mg Nanocrystals Prepared from Solution. *J. Am. Chem. Soc.* **2011**, *133* (28), 10679–10681.

(16) Johnson, N. J. J.; Lam, B.; MacLeod, B. P.; Sherbo, R. S.; Moreno-Gonzalez, M.; Fork, D. K.; Berlinguette, C. P. Facets and Vertices Regulate Hydrogen Uptake and Release in Palladium Nanocrystals. *Nat. Mater.* **2019**, *18* (5), 454–458.

(17) Christmann, K.; Schober, O.; Ertl, G.; Neumann, M. Adsorption of Hydrogen on Nickel Single Crystal Surfaces. *J. Chem. Phys.* **1974**, *60*, 4528–4540.

(18) Ye, J.; Zhao, Y.; Fang, Y.; Lin, H.; Bai, L. ScienceDirect Hydrogen Adsorption , Dissociation , and Diffusion on High-Index Mg (1013) and Their Comparisons with Mg (0001): A Systematic First-Principles Study. *Int. J. Hydrogen Energy* **2019**, *44*, 4897–4906.

(19) Ouyang, L.; Tang, J.; Zhao, Y.; Wang, H.; Yao, X.; Liu, J.; Zou, J.; Zhu, M. Express Penetration of Hydrogen on Mg(1013) along the Close-Packed-Planes. *Sci. Rep.* **2015**, *5*, 10776.

(20) Wentzcovitch, R. M. Hcp-to-Bcc Pressure-Induced Transition. *Phys. Rev. B* **1994**, *50* (14), 10358–10361.

(21) Howe, B. F. and J. M. *Transmission Electron Microscopy and Diffractometry of Materials*; Springer Science & Business Media, 2012.

(22) Saeki, R.; Ohgai, T. Effect of Growth Rate on the Crystal Orientation and Magnetization Performance of Cobalt Nanocrystal Arrays Electrodeposited from Aqueous Solution. *Nanomaterials* **2018**, *8* (8).

(23) Ghosh, S.; Gupta, R.; Ghosh, S. Effect of Free Energy Barrier on Pattern Transition in 2D Diffusion Limited Aggregation Morphology of Electrodeposited Copper. *Heliyon* **2018**, *4* (12), e01022.

(24) Rudman, P. S. Hydrogen-Diffusion-Rate-Limited Hydriding and Dehydriding Kinetics. *J. Appl. Phys.* **1979**, *50* (11), 7195–7199.

(25) Rudman, P. S. Hydriding and Dehydriding Kinetics. *J. Less-Common Met.* **1983**, *89*, 93–110.

(26) Holy, N. L. Reactions of the Radical Anions and Dianions of Aromatic Hydrocarbons. *Chem. Rev.* **1974**, *74* (2), 243–277.

(27) Cui, J.; Liu, J.; Wang, H.; Ouyang, L.; Sun, D.; Zhu, M.; Yao, X. Mg-TM (TM: Ti, Nb, V, Co, Mo or Ni) Core-Shell like Nanostructures: Synthesis, Hydrogen Storage Performance and Catalytic Mechanism. *J. Mater. Chem. A* **2014**, *2* (25), 9645–9655.

(28) Jiang, T.; Sun, L. X.; Li, W. X. First-Principles Study of Hydrogen Absorption on Mg(0001) and Formation of Magnesium Hydride. *Phys. Rev. B* **2010**, *81*, 035416.

(29) Pozzo, M.; Alfè, D.; Amieiro, A.; French, S.; Pratt, A. Hydrogen Dissociation and Diffusion on Ni- and Ti-

Doped Mg (0001) Surfaces. *J. Chem. Phys.* **2008**, *128*, 094703.

(30) Johansson, M.; Ostenfeld, C. W.; Chorkendorff, I. Adsorption of Hydrogen on Clean and Modified Magnesium Films. *Phys. Rev. B* **2006**, *74*, 193408.

(31) Sciences, E.; Street, G.; Wce, L.; Kingdom, U. Hydrogen Dissociation on Mg(0001) Studied via Quantum Monte Carlo Calculations. *Phys. Rev. B* **2008**, *78*, 245313.

(32) Vegge, T. Locating the Rate-Limiting Step for the Interaction of Hydrogen with Mg (0001) Using Density-Functional Theory Calculations and Rate Theory. *Phys. Rev. B* **2004**, *70*, 035412.

(33) Valiev, M.; Bylaska, E. J.; Govind, N.; Kowalski, K.; Straatsma, T. P.; Van Dam, H. J. J.; Wang, D.; Nieplocha, J.; Apra, E.; Windus, T. L.; De Jong, W. A. NWChem: A Comprehensive and Scalable Open-Source Solution for Large Scale Molecular Simulations. *Comput. Phys. Commun.* **2010**, *181* (9), 1477–1489.

(34) Stephen, P. J.; Devlin, F. J.; Chabalowski, C. F.; Frisch, M. J. Ab Initio Calculation of Vibrational Absorption. *J. Phys. Chem.* **1994**, *98* (45), 11623–11627.

(35) Kresse, G.; Furthmuller, J. Efficient Iterative Schemes for Ab Initio Total-Energy Calculations Using a Plane-Wave Basis Set. *Phys. Rev. B* **1996**, *54*, 11169.

(36) Perdew, J. P.; Burke, K.; Ernzerhof, M. Generalized Gradient Approximation Made Simple. *Phys. Rev. Lett.* **1996**, *77* (18), 3865–3868.

(37) Blöchl, P. Projector Augmented-Wave Method. *Phys. Rev. B* **1994**, *50* (24), 17953.

(38) Hjorth Larsen, A.; JØrgen Mortensen, J.; Blomqvist, J.; Castelli, I. E.; Christensen, R.; Dułak, M.; Friis, J.; Groves, M. N.; Hammer, B.; Hargus, C.; Hermes, E. D.; Jennings, P. C.; Bjerre Jensen, P.; Kermode, J.; Kitchin, J. R.; Leonhard Kolsbjerg, E.; Kubal, J.; Kaasbjerg, K.; Lysgaard, S.; Bergmann Maronsson, J.; Maxson, T.; Olsen, T.; Pastewka, L.; Peterson, A.; Rostgaard, C.; SchiØtz, J.; Schütt, O.; Strange, M.; Thygesen, K. S.; Vegge, T.; Vilhelmsen, L.; Walter, M.; Zeng, Z.; Jacobsen, K. W. The Atomic Simulation Environment - A Python Library for Working with Atoms. *J. Phys. Condens. Matter* **2017**, *29* (27), 273002.

(39) Henkelman, G.; Uberuaga, B. P.; Jónsson, H. Climbing Image Nudged Elastic Band Method for Finding Saddle Points and Minimum Energy Paths. *J. Chem. Phys.* **2000**, *113* (22), 9901–9904.

TOC

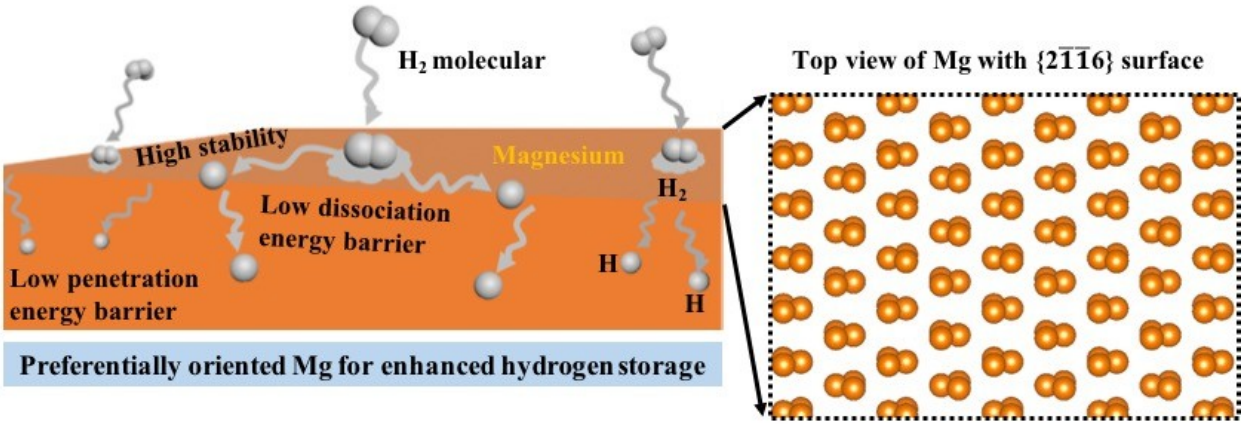
H2 molecular
Top view of Mg with {2$\bar{1}\bar{1}$6} surface
High stability
Magnesium
H2
Low dissociation
energy barrier
H
Low penetration
energy barrier
H
Preferentially oriented Mg for enhanced hydrogen storage